



Silicon photonic MEMS switches based on split waveguide crossings

Received: 5 July 2024

Accepted: 16 December 2024

Published online: 02 January 2025

Check for updates

Yinpeng Hu¹, Yi Sun¹, Ye Lu¹, Huan Li^{1,2,3}✉, Liu Liu^{1,2,3},
Yaocheng Shi^{1,2,3} & Daoxin Dai^{1,2,3}✉

The continuous push for high-performance photonic switches is one of the most crucial premises for the sustainable scaling of programmable and reconfigurable photonic circuits for a wide spectrum of applications. Conventional optical switches rely on the perturbative mechanisms of mode coupling or mode interference, resulting in inherent bottlenecks in their switching performance concerning size, power consumption and bandwidth. Here we propose and realize a silicon photonic 2×2 elementary switch based on a split waveguide crossing (SWX) consisting of two halves. The propagation direction of the incident light is manipulated to implement the OFF/ON states by splitting/combining the two halves of the SWX, showing excellent performance with low excess loss and low crosstalk over an ultrawide bandwidth. Both elementary switch and a 64×64 switch array based on Benes topology are fabricated and characterized, demonstrating great potential for practical scenarios such as photonic interconnect/routing, Lidar and spectroscopy, photonic computing, as well as microwave photonics.

The rapid development of Artificial Intelligence (AI) and Internet of Things (IoT) are driving explosive demands for ultrahigh-capacity data transmission and signal processing¹. Accordingly, it is required to develop sophisticated large-scale photonic integrated circuits (PICs) with high flexibility to be programmable and reconfigurable^{2–4}, where photonic switches of every scale (from 1×2 to M×N) are playing a key role to improve the utilization of the hardware resources as well as to reduce latency and energy consumption^{5,6}. Photonic switches have been demonstrated for various PICs in photonic interconnect/routing⁷, Lidar⁸ and spectroscopy⁹, photonic computing¹⁰, as well as microwave photonics^{11,12}.

For example, large-scale photonic switches are indispensable for implementing agile, flexible, and scalable optical packet/burst switching (OPS/OBS) in datacenters. In this case, the scale of the photonic switches is preferably to be as large as 64×64¹³. For AI deep neural networks (DNN), photonic interconnect based on large-scale photonic switches enables massive data exchange among enormous amounts (tens of thousands or even more) of memories and

processors, which avoids electronic interconnect with optical-electrical-optical (O-E-O) conversion and provides much broader bandwidths for data exchange¹⁴. The implementation of high-resolution focal-plane-switch-array (FPSA) lidars¹⁵ also requires a large number of switch pixels as many as ~10⁶. A large-scale photonic switch is usually constructed from 1×2 and 2×2 elementary switches connected into networks/arrays of a variety of topologies, such as Cross-Bar, Benes, and path-independent loss (PI-Loss), as well as their numerous variants. Given that there are hundreds of or more elements in cascade, it is important to achieve high-performance elementary switches with e.g., low excess losses and crosstalk across a broad photonic bandwidth. Otherwise, even small excess loss and crosstalk (especially coherent crosstalk) from each elementary switch will accumulate rapidly as the switch networks/arrays scale up, leading to unacceptable degradation of signal integrity^{16,17}. Although photonic switches with an ultrawide wavelength-band of hundreds of nanometers are highly desired for applications such as multiband wavelength-division-multiplexing (WDM) and digital Fourier

¹State Key Laboratory of Extreme Photonics and Instrumentation, College of Optical Science and Engineering, Zhejiang University, Hangzhou 310058, China.

²Jiaxing Key Laboratory of Photonic Sensing & Intelligent Imaging, Jiaxing 314000, China. ³Intelligent Optics & Photonics Research Center, Jiaxing Research Institute Zhejiang University, Jiaxing 314000, China. ✉e-mail: lihuany20@zju.edu.cn; dxdai@zju.edu.cn

transform spectroscopy⁹, they have been less reported and remain a major challenge. Also, the wavelength insensitivity often implies excellent fabrication tolerance, which is very important for realizing commercial large-scale photonic switches. Furthermore, power/energy consumption and footprints of the elementary switches are also potential limiting factors for further scaling up PICs. Finally, the overall robustness, including large tolerance for fabrication and electrical drive, excellent repeatability and stability, and long durability are all highly desired features for elementary switches. In summary, the continuous push for high-performance elementary switches with low excess loss, low crosstalk, large bandwidth, low power/energy consumption, compact footprint, and overall robustness, is one of the most crucial premises for sustainable PIC scaling as desired for many applications.

As for the operation principles, most elementary switches are realized with Mach-Zehnder interferometers^{18–22} (MZIs) or photonic resonators/cavities^{7,23–25}, for which two-beam or multi-beam interference is manipulated by introducing perturbative phase shift electro-optically or thermo-optically. Recently 32×32 silicon photonic switches with decent performances have been demonstrated using electro-optic (EO) MZIs²⁶ of Benes topology and thermo-optic (TO) MZIs²⁷ of PI-Loss topology. Moreover, 128×128 Benes switch array using EO MZIs is demonstrated as well, however, without characterization of the performance²⁸. Since the change of the refractive index due to the EO and TO effects is usually low (i.e., $\sim 10^{-4}$ or $\sim 10^{-3}$)^{29,30}, fundamental trade-offs among the footprint, the excess loss, the power consumption, and the bandwidth are inevitable. Specifically, silicon EO phase-shifters are generally millimeter-scale and lossy due to free carrier absorption³¹ (FCA). Although silicon TO phase-shifters can be as short as $< 100 \mu\text{m}$ and almost lossless, continuous thermal power supply of tens of mW is required²⁹. Alternatively, resonators/cavities can be employed to break the trade-off among the footprint, the excess loss and the power consumption, but at the price of narrow-band operations. Furthermore, due to the analog/continuous nature of the EO/TO phase shifts³², highly precise electrical drive is often required for digital switching. These phase shifters are also highly susceptible to the fabrication variations. Therefore, it is usually required to introduce sophisticated device characterizations, feedback control and stabilization schemes³³, which becomes almost infeasible for large-scale switches with more than ~ 100 input/output ports. More fundamentally, phase-shifting is intrinsically a wavelength-dependent physical process^{30,34}, prohibiting ultrawide operation bandwidths across hundreds of nanometers.

Another emerging type of elementary switches relies on the manipulation of mode coupling. This type of switching mechanism is well suited for micro/nano-electromechanical-system (MEMS/NEMS) actuation and transduction^{35–37}. Generally speaking, for almost all MEMS photonic devices, the basic idea is to mechanically move a certain part of the structure so that the light path or phase is manipulated. For example, previous MEMS photonic switches were often realized by introducing some mechanical displacement/deformation to make the waveguide structures be coupled or decoupled^{38–42}. For such type of switches, the electrostatic actuation consumes near-zero power in steady-states. MEMS switches based on directional couplers (DCs) has been demonstrated with low excess loss and low crosstalk^{38,41,43}. However, it is not suitable for large-scale arrays in practical applications due to the bandwidth limitation of $< 30 \text{ nm}$ and complex calibration caused by sensitivity to fabrication errors. Particularly, electrostatically-actuated vertical adiabatic couplers⁴⁴ (VACs) were demonstrated with low excess losses of 0.7 dB and high extinction ratio of 70 dB at the wavelength of 1500 nm . The demonstrated MEMS silicon photonic switch features a minimum footprint of $110 \mu\text{m} \times 110 \mu\text{m}$, a drive voltage of 65 V , low switching energy consumption of tens of pJ , switching speed of μs -scale, ultrawide bandwidth of hundreds of nanometers, and excellent fabrication tolerance.

Such high-performance elementary switches make it possible to realize unprecedented 240×240 and 128×128 Cross-Bar switches for interconnect⁴⁴ and Lidar applications⁴⁵, respectively. However, such VAC MEMS switches are essentially capable of only 1×2 switching operation and incapable of 2×2 switching operation⁴⁴, hence they are compatible with Cross-Bar topology only and inapplicable in many other topologies (such as Benes and PI-Loss). Due to this topological limitation, 57,600 (240^2) switch cells are required for the 240×240 array mentioned above, which is 30 times of a 256×256 Benes switch array with 1,920 cells. Such enormous numbers of switch cells usually significantly complicate the packaging and control of the switch array. A special approach of utilizing the hysteresis characteristics of VAC switches enables a row/column addressing scheme⁴⁶ to effectively reduce the pad scale from N^2 to $2N$, while this approach only allows the switch cells to be switched one-after-one, as discussed in ref. 46. Moreover, because the Cross-Bar topology requires all the switch cells work properly to ensure proper function, such enormous numbers of switch cells are still undesired because they may compromise the yield and increase the risk of array damage. Also, the VAC design requires an additional polysilicon layer, which is incompatible with most standard silicon photonic foundry processes currently accessible⁴⁴. Accordingly, 2×2 elementary switches based on horizontal adiabatic couplers (HACs) have been demonstrated for 8×8 Cross-Bar switches⁴⁷, where only a single silicon layer on a standard silicon-on-insulator (SOI) wafer is needed and thus low-cost standard foundries can be used. Unfortunately, the measured crosstalk in the ON state is still as high as $\sim -10 \text{ dB}$ across a bandwidth of $\sim 110 \text{ nm}$ and the switching speed is as slow as $\sim 36.7 \mu\text{s}$.

Here we propose a MEMS elementary switch on standard SOI by manipulating the mode propagation, as shown in Fig. 1a, b, which is very different from the scheme of manipulating the mode interference or mode coupling. Specifically, the proposed 2×2 silicon photonic MEMS switch consists of a waveguide crossing that is split into two halves, each of which alone functions as a 90° multimode waveguide reflector based on total internal reflection (TIR). When the two halves split into two waveguide reflectors, the input light turns 90° into the adjacent waveguide on the same side, and the switch is in the OFF state, shown in Fig. 1a. On the other hand, when the two halves combine into one waveguide crossing, the input light propagates straight and the switch is in its ON state, shown in Fig. 1b. For the present silicon photonic MEMS switch based on a split waveguide crossing (SWX), one half is stationary, while the other half is movable, actuated by a compact MEMS electrostatic comb, as shown in Fig. 1c. Such an elegant and unique structure design can drastically modify the mode propagation with an ultra-compact reconfigurable photonic structure, particularly implementing a 2×2 photonic switch (instead of the 1×2 type). Compared with the work on single-pole single-throw (SPST)⁴⁸ and the simulated single-pole double-throw (SPDT)⁴⁹ switches based on movable waveguides, the present 2×2 SWX switch features distinct operation principles and superior feasibility, performance, and scalability. Compared with the 1×2 VAC switch⁴⁴, the present 2×2 SWX switch proposed here is ~ 10 times more compact (for the area of the photonic structure), two-orders more energy-efficient (See Supplementary Section 8), and fully applicable in versatile topologies, with both intricate photonic and MEMS structures fabricated within a single layer of silicon on a standard SOI wafer (See Supplementary Section 1). Here the present 2×2 SWX switch features excellent performance with low excess loss of $0.1\text{--}0.52$ ($0.1\text{--}0.47$) dB and low crosstalk of <-37.1 (-22.5) dB over an ultrawide bandwidth of $1400\text{--}1700 \text{ nm}$ for the OFF (ON) states in simulation, while in experiment, excess loss of $0.12\text{--}0.4$ ($0.54\text{--}0.76$) dB and crosstalk of <-44 (-24.1) dB over the bandwidth of $1420\text{--}1600 \text{ nm}$ (limited by the input/output grating couplers) for the OFF (ON) states have been measured. The switch features a total footprint of $95 \mu\text{m} \times 100 \mu\text{m}$ ($23 \mu\text{m} \times 23 \mu\text{m}$ for the SWX alone), acceptably low drive voltage threshold of $\sim 20 \text{ V}$, maximum drive

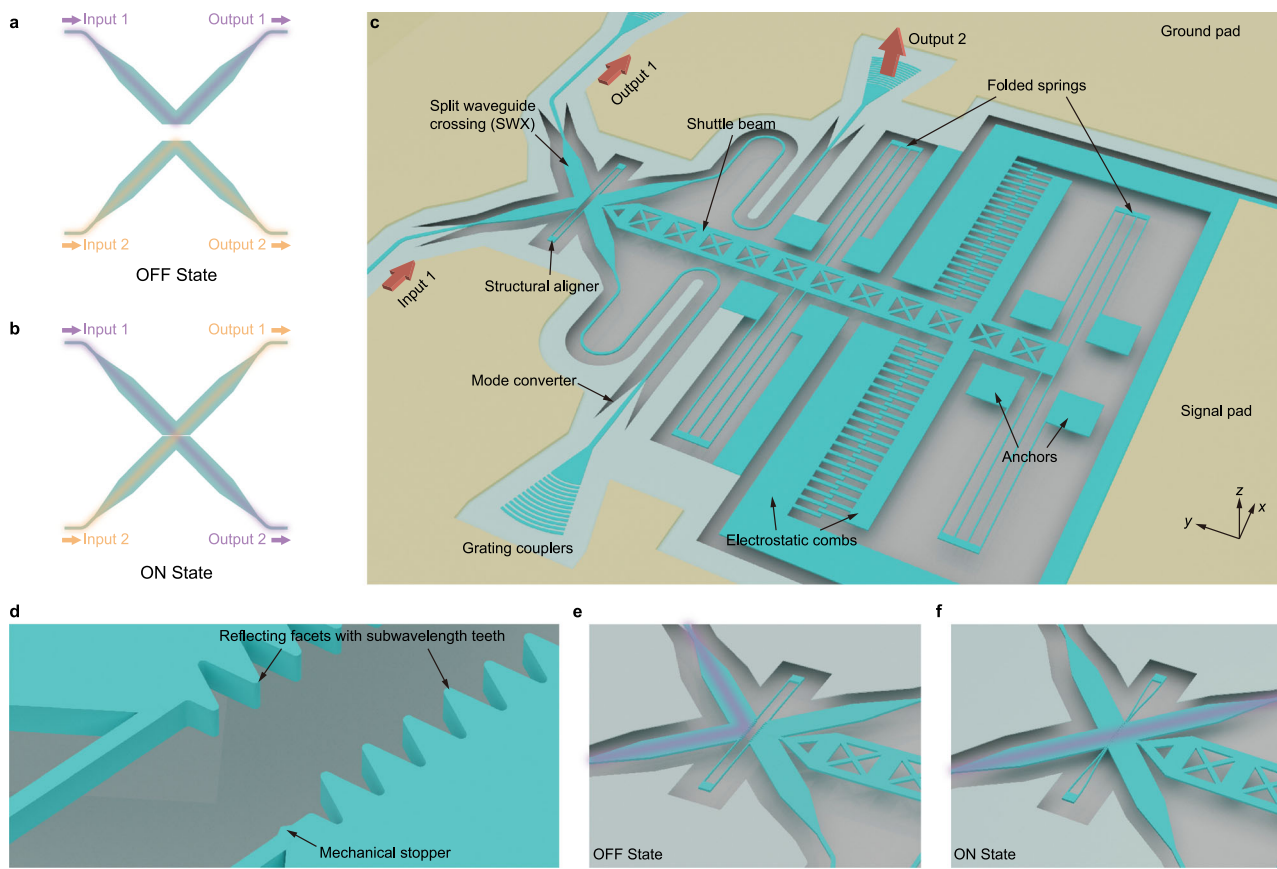


Fig. 1 | Schematic illustrations of the switch. **a, b** The split waveguide crossing (SWX) in the OFF and ON state, respectively. **c** Schematic diagram of the designed photonic and electromechanical structures. **d** Close-up view of the subwavelength-

teeth (SWT) and mechanical stopper. **e, f** The SWX with SWT reflecting facets of the switch in the OFF and ON state, respectively.

voltage rating beyond -24 V, near-zero steady-state power consumption, low switching energy of sub-pJ, switching speed of μs -scale, and durability beyond 10⁹ switching cycles (no observable performance degradation). Note that any voltage between the threshold and the maximum rating can drive the switch digitally from the OFF state to the ON state with identical performances. Such a large tolerance warrants robust drive schemes for large-scale switch networks/arrays. Note that the crosstalk in the OFF state can be much lower by splitting the two halves of the SWX more, at the price of higher drive voltage. With such high-performance 2 × 2 elementary switches, a 64 × 64 silicon photonic switch using Benes topology has been fabricated (the largest Benes switch array based on photonic MEMS reported to date) and characterized to validate the capability of the SWX switches to further scale up for practical applications such as photonic interconnect/routing, Lidar and spectroscopy, photonic computing, as well as microwave photonics.

Results

Device design

The proposed 2 × 2 silicon photonic MEMS switch operates with a unique SWX, which can be reconfigured electrostatically, as shown in Fig. 1. The present SWX consists of two halves configured initially with a sufficiently large air gap between them, hence they serve as compact waveguide corner-bends enabling total internal reflection (TIR). In this case the switch is in its OFF state and the input light turns 90° into the output waveguide on the same side, as shown in Fig. 1a. In order to guarantee low crosstalk in the OFF state, initially the air gap should be much larger than the Goos-Hanchen displacement, which is typically hundreds of nanometers for the telecom wavelength-band. On the other hand, when the two halves of the SWX are reconfigured

electrostatically to be with a near-zero gap in-between, the structure effectively becomes a near-perfect waveguide crossing based on self-imaging, in which case the switch works in the ON state and the input light propagates straightly into the output waveguide on the other side, as shown in Fig. 1b.

To implement the proposed 2 × 2 silicon photonic MEMS switch, we have devised intricate and coordinated designs of photonic and MEMS structures within a single layer of silicon on standard SOI wafers, as shown in Fig. 1c. Both halves of the SWX are suspended and connected with input/output waveguides. One half is stationary, fixed by the rigid triangle formed by the straight input/output waveguides. Meanwhile, the other half is movable due to the flexibility of the meandering input/output waveguides when actuated in the y direction by a compact MEMS electrostatic comb via a shuttle beam. The two halves are also connected with a pair of aligners to minimize their misalignment in the z and x directions (See Supplementary Section 3). Otherwise, misalignment often occurs due to the residual stress in the SOI wafer and/or asymmetric fabrication variations in the suspended silicon structures, and may lead to significant performance degradation for the ON state, when the two halves of the SWX are supposed to engage. The shuttle beam is perforated to achieve better rigidity with less mass, hence less inertia and faster switching response (See Supplementary Section 5). The shuttle is suspended from two pairs of folded springs, which are flexible in the y direction but are rigid in the x direction to minimize the undesired lateral displacement (See Supplementary Section 3). Between these two pairs of folded springs, there are a pair of movable electrostatic combs fixed to the shuttle beam. When a drive voltage is applied, the movable comb pair is attracted toward the stationary comb pair by the electrostatic force in the +y direction, thereby engaging the SWX switch, which is now in its

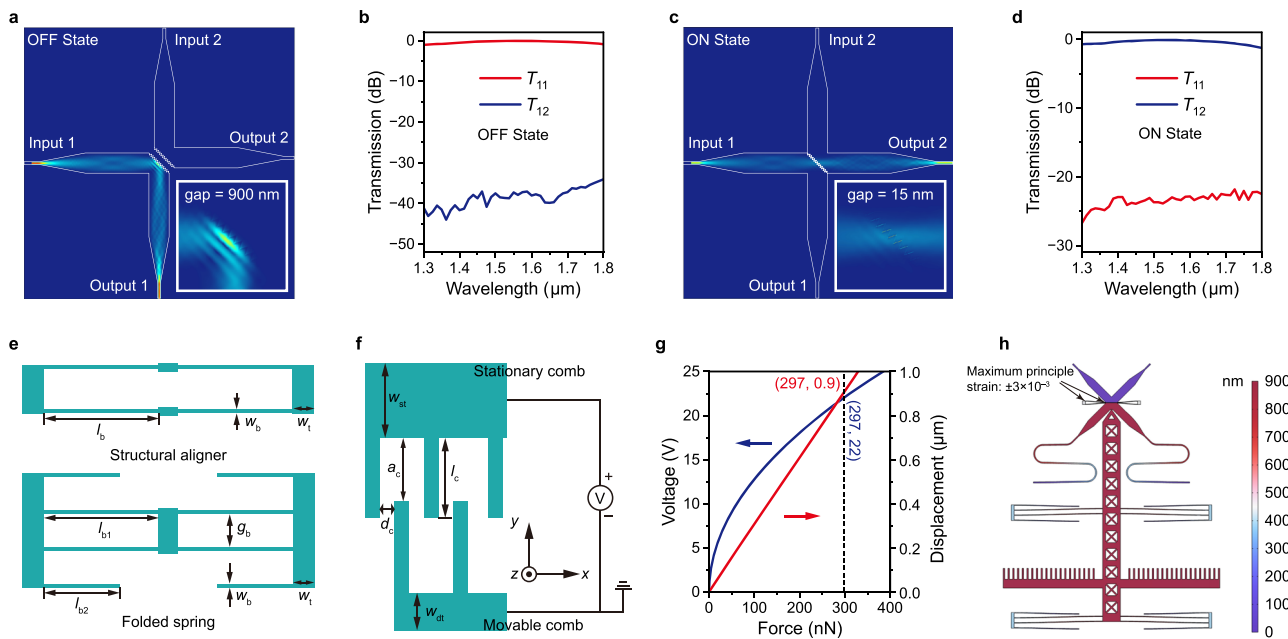


Fig. 2 | Design of the switch based on split waveguide crossings. Simulated light propagation diagrams with transmission spectra of the switch in the OFF state (**a**, **b**) and ON state (**c**, **d**), respectively. The inset of **a** and **c** shows the close-up view around the reflecting facets. Schematic diagram of the structural aligner, folded

spring (**e**), and electrostatic comb (**f**). **g** Simulated electrostatic force arisen by different voltage and corresponding displacement of the movable mechanical structures. **h** Displacement of the movable mechanical structures in the ON state.

ON state. Meanwhile, when the drive voltage is removed, the movable comb pair is pulled back to its initial position by the restoring force (in the $-y$ direction) of the folded springs, thereby disengaging the SWX switch, which is now in its OFF state. Here the drive voltage is only applied on the stationary comb, while all other silicon structures (especially the suspended structures) are readily connected in the silicon layer and always grounded. In such a design, neither the mechanical structures nor their movement compromises the photonic performance of the rigid SWX or disrupt the input/output photonic waveguides.

It should be noted that the two halves of the SWX should never directly contact with a zero gap. Otherwise, the strong van der Waals forces between them will lead to destructive stiction problems, hence switch failure (See Supplementary Section 2). Therefore, a small bump is incorporated on both sides of the movable reflecting facet as a mechanical stopper, which can prevent large-area contact for the ON state. As a result, the contact area between the stopper and the stationary reflecting facet is small enough to prevent stiction. On the other hand, for the ON state, it is desired to minimize the gap between the two SWX halves to achieve optimal performances, which imposes stringent requirements on the fabrication precision of the stoppers. Furthermore, one should note that the sidewalls of the etched silicon layer are not perfectly vertical, which prevents the two SWX halves from engaging properly. Instead, it often results in an unacceptably large wedge-shaped gap (See Supplementary Section 2). To address these pragmatic issues, here we introduce refractive-index engineering by incorporating subwavelength-tooth (SWT) structures on both reflecting facets, as shown in Fig. 1d-f. With such a unique structural design, the two SWX halves can properly engage in the ON state because their SWT facets are matched well even when a nm-scale gap is introduced between them as desired to prevent stiction. In contrast, for the OFF state, the SWT facets are well equivalent to a thin layer with a gradient refractive index profile, still guaranteeing TIR for the incident light.

The photonic structures are designed optimally with three-dimensional (3D) finite-difference time-domain (FDTD) simulations. For the designed SWX, we choose the waveguide width $w = 2.68 \mu\text{m}$

and the total length $L = 19.54 \mu\text{m}$. Taking the fabrication capability and the switch performance into consideration, the SWT design is finalized with a period of 290 nm and a depth of 300 nm. Note that the condition of subwavelength operation might not be satisfied as the wavelength decreases. Therefore, the SWT introduces performance degradation in short wavelengths, introducing the limitation to the ultra-broad bandwidth. To obtain low crosstalk in both states, the air gap in the OFF state is designed to be 900 nm while the height of the mechanical stoppers (corresponding to the air-gap width in the ON state) is designed to be 15 nm (See Supplementary Section 2). Figure 2a shows the simulated light propagation in the designed SWX in the OFF state, where the incident light is reflected to the output port on the same side by the SWT facet. The corresponding transmission spectra are shown in Fig. 2b, featuring an excess loss of 0.1–0.52 dB and crosstalk $<-37.1 \text{ dB}$ over an ultrawide bandwidth of 1400–1700 nm. The self-imaging imperfection as well as the ignorance of Goos-Hanchen displacement contributes to the simulated excess loss in OFF state, which shows slight wavelength dependence and can be further reduced by improving the SWX design. For the SWX operating in the ON state with a tiny gap of 15 nm induced by the mechanical stopper, the simulated light propagation is shown in Fig. 2c, where the incident light propagates straightly across the waveguide crossing area with a low excess loss and a high extinction ratio. Figure 2d shows the corresponding transmission spectra, featuring an excess loss of 0.1–0.47 dB and crosstalk of $<-22.5 \text{ dB}$ over the same bandwidth. The self-imaging imperfection caused by the mechanical stoppers contributes to the simulated excess loss in ON state primarily, which shows slight wavelength dependence as well. Evidently, the incorporation of the SWX aligner pair and the shuttle beam does not disturb the light propagation in the SWX, as shown in Fig. 2a, c, because the optical fields are negligible at the locations where these mechanical structures are connected. In addition, the elastic deformation of the mechanical structures, especially the meandering waveguides, causes no additional excess loss as well.

Figure 2e shows the schematic diagram of the springs used here, designed with high rigidity in the x direction and high flexibility in the y

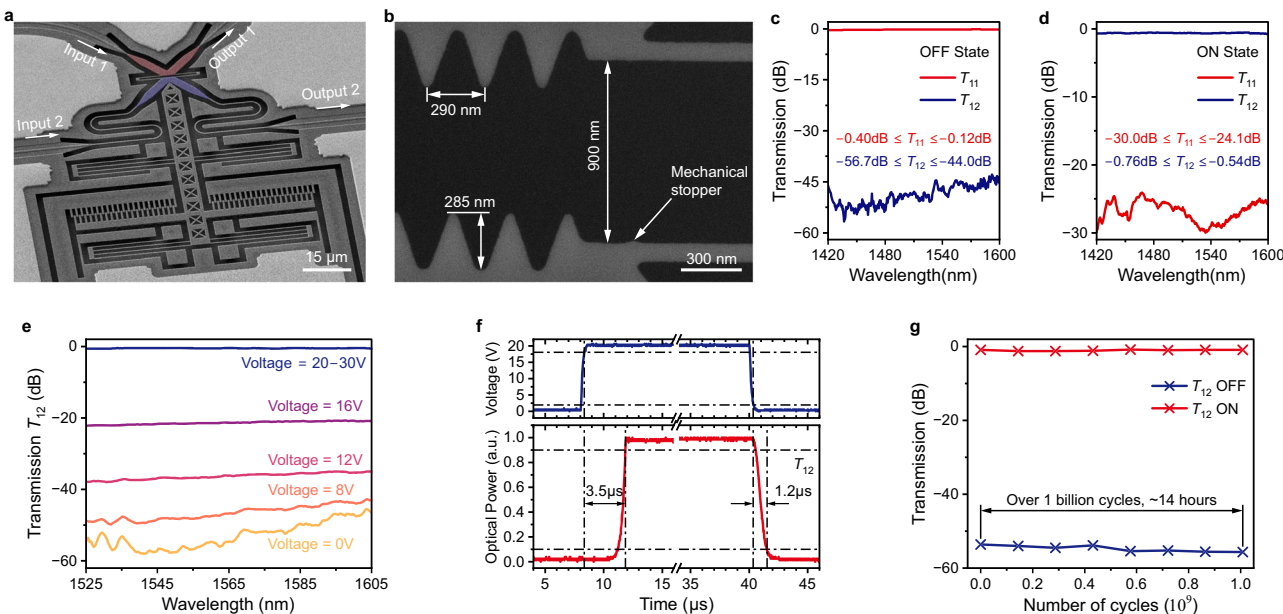


Fig. 3 | Fabrication and measurement results of the device. **a** Perspective scanning electron microscope (SEM) image of the fabricated device. Stationary and movable halves of the split waveguide crossing are highlighted with red and blue, respectively. **b** A close-up view of the reflecting facets and mechanical stopper. Period and depth of the subwavelength-teeth were measured. **c, d** Transmission T_{11}

and T_{12} in the OFF and ON state, respectively. **e** Transmission T_{12} with different actuation voltages. The threshold voltage is measured to be 20 V and the maximum drive voltage rating is beyond 30 V. **f** Temporal response of the switch. **g** Durability test of the switch. The switch was turned on and off for over 1 billion times and the optical transmission T_{12} at 1550 nm was recorded.

direction (See Supplementary Section 3). Figure 2f shows the schematic diagram of the electrostatic combs. The width w_{st} of the stationary comb handle is designed to be 6 μm, which is sufficiently wide to remain anchored to the buried oxide (BOX) layer during the MEMS releasing process. The width w_{dt} of the movable comb handle is designed to be 3 μm, which is sufficiently narrow to be completely released, meanwhile sufficiently rigid to avoid bending due to the electrostatic and elastic force. To ensure excellent stability for the entire MEMS structures in the x direction, the electrostatic force generated in the x direction should be minimized by meticulously designed comb fingers. Here the overlap length ($l_c - a_c$) and the gap width d_c are designed to be 200 nm and 300 nm, respectively (See Supplementary Sections 4 and 6). Figure 2g shows the electrical and mechanical simulation results using finite element method (FEM). The red line shows the linear relationship between the driving force and the displacement. The elastic deformation of the mechanical structures follows Hooke's law, with a spring constant of -0.33 N/m. The blue curve shows the quadratic relationship between the driving force generated by the electrostatic combs and the applied voltage. According to the electrical and mechanical simulation results, the threshold voltage is -22 V for the designed SWX switch with an initially 900-nm-wide gap in the OFF state. Finally, the entire MEMS structure design has been verified with the FEM simulation of the ON state shown in Fig. 2h, where the maximum tensile and compressive principal strain of $\pm 3 \times 10^{-3}$ occurs at the SWX aligners, well below the damage threshold of silicon (See Supplementary Section 3). To analyze the frequency response of the device, the fundamental resonance frequency of the mechanical structures is estimated to be 0.14 MHz as a simple harmonic oscillator. Such a resonance frequency indicates that the highest switching frequency is up to ~100 kHz, enabling μs-scale switching speed (See Supplementary Section 5). Resistance of the device against mechanical shocks are estimated in theory as well (See Supplementary Section 7). The results show that accelerations up to 100 g (g is the gravitational acceleration) only cause minor disturbances to the structures.

Experimental results

The SWX switch device was fabricated with electron-beam lithography (EBL) process in which proximity effect correction (PEC) is involved. Figure 3a shows a scanning electron microscope (SEM) image of the device, where the stationary and the movable SWX halves are highlighted with red and blue, respectively. All structures are suspended except the stationary electrostatic comb and the anchors. The SWX itself has an ultra-compact footprint of 23 μm × 23 μm, while the total footprint including the MEMS actuator is 95 μm × 100 μm. As shown by the close-up view of the SWT structures and mechanical stoppers in Fig. 3b, the period and depth of the SWT were measured to be 290 nm and 285 nm approximately, while the height of the mechanical stopper was measured to be about 15 nm. The movable half-SWX is 900 nm away from the stationary one in the OFF state as designed. When the switch is turned on, the movable half-SWX is pushed toward the stationary one by the MEMS actuator and the gap between the two halves is precisely defined to be 15 nm by the mechanical stoppers.

For precise measurement of the excess loss, ten cascaded elementary switches were measured and averaged. Figure 3c shows the measured transmission spectra T_{11} and T_{12} at the two output ports in the OFF state, exhibiting a low excess loss of 0.12–0.4 dB for T_{11} and a low cross talk of <-44 dB for T_{12} in the measured wavelength range of 1420–1600 nm (further broadband measurement is limited by the efficiency of the grating couplers used here). Figure 3d shows the measured transmission spectra T_{11} and T_{12} at the two output ports in the ON state, where the excess loss of T_{11} is 0.54–0.76 dB and the crosstalk of T_{12} is <-24.1 dB in the wavelength range of 1420–1600 nm. For the OFF state, the excess loss agrees well with the simulated results, while for the ON state the excess loss is slightly higher due to fabrication imperfection of the SWX and the SWT. The measured crosstalk in the ON state agrees with the simulated value (<-22.5 dB), indicating that the SWX is engaged tightly with a gap of <15 nm and the sidewall inclination is small.

To further characterize the steady-state switching performance, transmission spectra T_{12} with different drive voltages were measured and shown in Fig. 3e. The threshold voltage was measured to be 20 V,

which agrees well with the simulation result of 22 V. The switch remains in the ON state without damage with a drive voltage up to 30 V, indicating a maximum drive voltage rating beyond 30 V. Because the actual maximum rating cannot be obtained without damaging the device, we refrained from such measurements. Note that any voltage between the threshold and the maximum rating can drive the switch digitally into its ON state with identical performances, as shown in the spectra measured with the drive voltage of 20–30 V in Fig. 3e. Such a large tolerance warrants robust drive schemes for large-scale switch arrays. The temporal response of the switch was measured by applying a square-wave pulse, as shown in Fig. 3f. The measured ON and OFF switching time (to 90% power and to 10% power) are respectively ~3.5 μs and ~1.2 μs. Note that a lower spring constant is preferred for achieving a lower threshold voltage, which however compromises the switching speed. For the ON switching, the movable half-SWX needs to travel ~600 nm forward (+y direction) from the initial OFF position to achieve sufficient optical power redirection from one half-SWX to the other, while for the OFF switching, the movable half-SWX only needs to travel ~300 nm backward (-y direction) from the ON position to stop the optical power redirection. Therefore, the OFF switching is faster than the ON switching. In order to test the durability of the SWX switch, we operated the switch for over one billion cycles with a square-wave voltage at 20 kHz. The measured transmission T_{12} at 1550 nm in the OFF and ON states are shown in Fig. 3g. Here the cross marks represent the measured transmission every two hours, exhibiting no performance degradation during the 14-hour test (See Supplementary Section 10). Finally, the SWX switch was held in the ON state over one hour without stiction (at the mechanical stoppers) or performance degradation.

Based on the 2×2 SWX switch described above, a 64×64 switch array using Benes topology was designed and fabricated by manual EBL process. To our best knowledge, this is the largest Benes switch array based on photonic MEMS reported to date. The switch array consisting of 352 switch cells has a footprint of $10\text{ mm} \times 5.3\text{ mm}$, as shown in Fig. 4a. Figure 4b, c, shows the close-up view of the switch cell and the waveguide connection shuffle. As shown in Fig. 4d, waveguides in the connection shuffles are broadened to reduce propagation loss and bent in Euler curve shape⁵⁰ to reduce footprint as well as suppress high-order modes (See Supplementary Section 12). Meanwhile, varied-width multimode interference (MMI) waveguide crossings⁵¹ are used in the connection shuffle to achieve low-loss and low-crosstalk propagation (See Supplementary Section 12). Grating couplers are used to access the input/output ports. The fabricated switch array was characterized with a pair of 66-channel fiber arrays and a pair of electrical probes (See Supplementary Section 13). The switch array in the initial all-OFF state (all 352 switch cells are OFF) was characterized by coupling light into the 64 input ports sequentially, and the measured transmission spectra T_{ij} ($i, j = 1, \dots, 64$) are shown in Fig. 4e. The maximum crosstalk of the leakage paths (T_{ij} with $i \neq j$) is 35 dB lower than the minimum transmission of the optical paths (T_{ij} with $i = j = 1, \dots, 64$) over the C band, exhibiting high crosstalk suppression. The excess losses of the 64 optical paths at the center wavelength of 1550 nm are shown in Fig. 4f by the blue rings. Notably, among the 64 optical paths, there are 6 paths ($i = j = 5, 21, 22, 48, 54, 55$) exhibiting conspicuously higher losses, as denoted by the red crosses in Fig. 4f. These elevated losses are attributed to specific fabrication defects that were inadvertently introduced during the manual EBL process (See Supplementary Section 12). To avoid confusion between defective optical paths and leakage paths, transmission spectra of these six defective optical paths are excluded in Fig. 4e. The excess losses of the 58 intact optical paths vary from 8.0 dB to 12.6 dB at the wavelength of 1550 nm. Meanwhile, we estimate the excess losses to be 5.2–11.7 dB, as the red rings show in Fig. 4f, according to our systematic experimental characterizations of the excess/propagation loss of the switch cells, as well as the waveguides of different widths, varied-width MMI waveguide crossings and Euler bends in the connection shuffles of the

Benes array (See Supplementary Section 11). Some discrepancies between the measured and estimated excess losses of the 58 intact optical paths are attributed to some slight fabrication defects, variations of the grating couplers (See Supplementary Section 11), inter-channel variations of the fiber arrays and the random particulate contamination directly on top of the silicon structures. Since the switch cells were electrically addressed by a pair of probes manually in the experiment, further measurement was limited to 32 specific states with single-ON switching (all switch cells are OFF except the selected one). Here the 32 switch cells in the center stage of the Benes array were switched ON sequentially, and the measured ON/OFF transmission spectra of the corresponding output ports are shown in Fig. 4g, exhibiting extinction ratios > 38 dB over the C band, with the results from four defective paths excluded (See Supplementary Section 12).

Discussion

Immunity to thermomechanical displacement noise

Thermomechanical displacement noise is present in any mechanical structures at finite temperature, and is most pronounced for nanomechanical structures near eigenmode (resonance) frequencies^{52–54}. Nevertheless, the effect of such noise on the SWX switch performance is negligible. For the ON state, the two SWX halves engage, such that the air gap in-between is mechanically fixed, even if the entire suspended structures are undergoing random thermomechanical motion. For the OFF state, the two SWX halves disengage, such that the air gap in-between is orders of magnitude larger than the thermomechanical displacement of the two SWX halves. Therefore, in neither of the two states, the displacement noise can be transduced onto the photonic signals. The same arguments apply to displacement noise of other origins.

Topology and scalability

Note that our 2×2 elementary switch has two input ports and two output ports, which is totally different from and much more versatile than those 1×2 switches that are limited to the Cross-Bar topology. Utilization of the present 2×2 elementary switch enables highly flexible large-scale switch network/array designs with various topologies such as Benes, PI-Loss and Cross-Bar. Note that all the array topologies feature specific advantages and disadvantages, therefore, the compatibility with various topologies is beneficial, so that it is possible to make best use of the advantages and avoids the disadvantages by choosing different topologies flexibly for different applications. For an $N \times N$ switch array with the Cross-Bar topology, signals transmitted from any input port to any output port pass only one elementary switch that is in the ON state. Accordingly, if the elementary switches work with low losses in the OFF state (which can be achieved in most cases), the total loss can be low when low-loss waveguide crossings are used, which is a unique advantage. However, for the Cross-Bar topology, N^2 elementary switches are required for an $N \times N$ switch array. The number of elementary switches increases quickly as the port counts scale up, which may compromise the yield and increase the risk of array damage. Furthermore, for switches without hysteresis characteristics, hence the unique row/column addressing scheme of the VAC switch⁴⁶ is not applicable, switch arrays with such enormous switch numbers may require challenging and cumbersome packaging and a sophisticated control system. In contrast, when using the Benes topology, one only needs $N(\log_2 N - 0.5)$ elementary switches for an $N \times N$ switch array. In this case, the total number of elementary switches can be minimized, which may significantly increase the yield and simplifies the packaging and the control system. In addition, for Benes topology, there are only $2\log_2 N - 1$ elementary switches (ON or OFF) in cascade for any optical paths⁵⁷, resulting in acceptable accumulated excess loss (compared with that N switch cells in cascade are needed for Cross-Bar topology). In light of the excellent scalability of the Benes topology, it is our on-going effort to develop a large-scale $N \times N$ switch

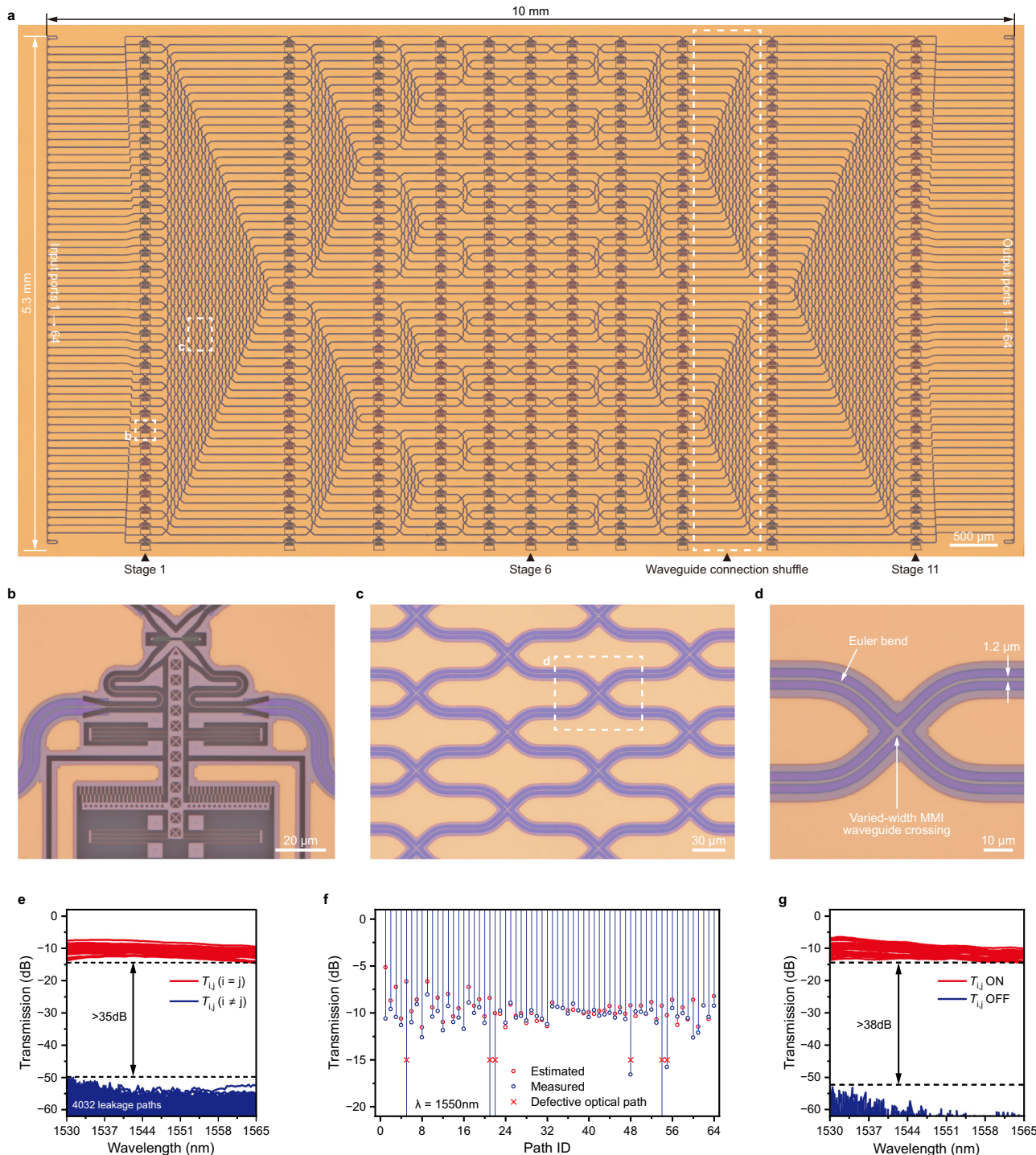


Fig. 4 | Fabrication and measurement results of the 64×64 switch array. **a** The optical microscope image of the 64×64 switch array. **b, c, d** Close-up view of a switch cell, connection shuffle (rotated by 90°) and varied-width multimode interference waveguide crossing, respectively. **e** The measured transmission T_{ij} of

the switch array in the all-OFF state. **f** Estimated and measured excess loss of the 64 optical paths in the all-OFF state at 1550 nm. **g** The measured transmission T_{ij} in the OFF/ON states of corresponding output ports with a single switch cell in the center stage turned on.

with e.g., $N = 128$ or more to meet the demands in various applications, especially photonic interconnect/routing and photonic computing.

Interfacing strategies

For MEMS switch arrays, the electrical pads are usually spread out across the entire layout because both the pads and wires are evaporated on the silicon directly, which requires electrical isolations, and thus the routing space of electrical wires is greatly constrained. The

interfacing of Benes switch array, which minimizes the number of pads effectively, can be readily implemented with mature technologies such as electrical feedthrough⁵⁵ and flip-chip bonding⁵⁶, both of which are compatible with standard silicon photonic foundry processes.

Compatibility with foundry processes

As described above, the fabricated reflecting-facets are not perfectly vertical in most cases, which leaves a wedge-shaped air gap between

the engaged SWX halves. Therefore, the SWT structure is introduced to alleviate the performance degradation due to the small air gap when the SWX switch is ON. For the fabricated devices in this paper, the SWT is designed with a period of 290 nm and a depth of 300 nm to achieve high performances. Note that such SWT with a relatively high aspect ratio (depth/period) of 300/290 cannot be fabricated yet by most commercial standard silicon photonic foundries with a minimum feature size of 130 nm or 180 nm (130/180-nm processes). Fortunately, there are a few advanced foundries with the minimum feature size of 90 nm and below available, which are potentially capable of fabricating the SWT. For the mechanical stopper even with tinier size than the SWT, it is easier to be fabricated in standard silicon photonic foundries due to its low lateral aspect ratio. In this paper all the devices were fabricated with EBL for experimental verification.

Alternatively, if the fabrication can be improved to further reduce sidewall inclination, a smaller air gap can be achieved for the SWX in the ON state, such that shallower SWT can be used for the reflecting facet. For the ideal case with zero air gap, excellent switch performance can be achieved even with flat reflecting facets (without SWT), which can be fabricated by a regular foundry with 130/180-nm processes for silicon photonics. Since it is nontrivial to consistently fabricate perfectly vertical silicon sidewalls, and zero gap is not allowed to avoid stiction, a feasible compromise is to push for gap widths less than 10 nm. In this case, excellent switch performance can still be obtained in the ultrawide bandwidth of 1400–1700 nm even when the SWT depth is reduced to 200 nm (See Supplementary Section 2), requiring the sidewall tilt angle to be $<1.5^\circ$ (which is possible with a well-calibrated etching process). Accordingly, such SWT can be fabricated compatibly with commercial standard silicon photonic foundries with low-cost 130-nm or even 180-nm processes.

As it is well known, both the waveguide propagation loss and the waveguide-crossing loss are critical sources for the Benes-topology array. When using commercial standard foundries, the propagation loss of the 600-nm-wide silicon photonic waveguides can be as low as 1.1 dB/cm or less, which is six times smaller than the loss of our silicon photonic waveguide fabricated with the manual EBL process. Meanwhile, as demonstrated in our previous work, the excess loss of the varied-width MMI waveguide crossings can be reduced to <10 dB⁵¹ with standard silicon photonic foundries. As a result, the total excess loss of the 64×64 array can be reduced to 6.3 dB in average and that of a 128×128 array can be expected as 9.1 dB (See Supplementary Section 12), such that the SWX switch will become a highly viable solution for large-scale silicon photonic switches for a broad spectrum of practical applications such as photonic interconnect/routing, Lidar and spectroscopy, photonic computing, as well as microwave photonics.

Methods

Fabrication of the device

The devices were fabricated on commercial SOI wafers (SOITEC) with a 220-nm-thick top silicon layer and a 2-μm-thick BOX layer. First, the ridge waveguides and strip waveguides were patterned with EBL, followed by the processes of 150-nm shallow etching and 220-nm full etching respectively. Second, metal electrodes (50-nm-thick chrome and 300-nm-thick gold films) were patterned with photolithography, followed by E-beam evaporation and lift-off processes. Finally, the suspended structures of the devices were released from the BOX by hydrofluoric vapor etching. The fabrication process for our device is not complicated and fully compatible with commercial standard silicon photonic foundries as well as standard silicon photonic MEMS platform.

Measurement of the device

Both the 2×2 elementary switch and the 64×64 Benes switch array were measured on a fiber-to-chip coupling platform (See

Supplementary Section 13). An amplified spontaneous emission laser (1520–1610 nm) and a super-luminescent diodes (1250–1650 nm) were used as the light source and the drive voltage signals were applied to the devices through direct-current probes. All the optical transmission spectra were measured with an optical spectrum analyzer (OSA, Yokogawa, AQ6370D). For the measurement of the elementary switch, a pair of fibers were used to couple the optical signal. The fiber-to-chip coupling loss was measured to be ~5 dB. In the ON/OFF optical transmission spectra measurement, the drive voltage was generated by a sourcemeter (Keithley 2400). The square-wave voltage for the temporal response measurement and the durability measurement was generated by a signal generator (SIGLENT SDG1032X). In the temporal response measurement, light output from the switch was measured with a photodiode (Newport 2053) and an oscilloscope (Tektronix, TBS1000C). For the measurement of the 64×64 switch array, a pair of 66-channel fiber array (spaced 80 μm, angled 8°) was used to couple the optical signal. To measure the 4096 transmission spectra of the Benes switch in its initial (all-OFF) state, a pair of commercial 1×64 optical switches were used to perform automatic measurements (See Supplementary Section 13).

Data availability

Data underlying the results presented in this paper are available from the authors upon request. Source data are provided with this paper.

References

- Cheng, Q., Bahadori, M., Glick, M., Rumley, S. & Bergman, K. Recent advances in optical technologies for data centers: a review. *Optica* **5**, 1354–1370 (2018).
- Bogaerts, W. et al. Programmable photonic circuits. *Nature* **586**, 207–216 (2020).
- Pérez-López, D., López, A., DasMahapatra, P. & Capmany, J. Multi-purpose self-configuration of programmable photonic circuits. *Nat. Commun.* **11**, 6359 (2020).
- Kim, D. U. et al. Programmable photonic arrays based on micro-electromechanical elements with femtowatt-level standby power consumption. *Nat. Photonics* **17**, 1089–1096 (2023).
- Cheng, Q., Rumley, S., Bahadori, M. & Bergman, K. Photonic switching in high performance datacenters. *Opt. Express* **26**, 16022–16043 (2018).
- Chen, X., Lin, J. & Wang, K. A Review of Silicon-Based Integrated Optical Switches. *Laser Photon. Rev.* **17**, 2200571 (2023).
- Vlasov, Y., Green, W. M. J. & Xia, F. High-throughput silicon nanophotonic wavelength-insensitive switch for on-chip optical networks. *Nat. Photonics* **2**, 242–246 (2008).
- Cao, X., Qiu, G., Wu, K., Li, C. & Chen, J. Lidar system based on lens assisted integrated beam steering. *Opt. Lett.* **45**, 5816–5819 (2020).
- Kita, D. M. et al. High-performance and scalable on-chip digital Fourier transform spectroscopy. *Nat. Commun.* **9**, 4405 (2018).
- Yan, F. et al. On the performance investigation of a fast optical switches based optical high performance computing infrastructure. *Computer Netw.* **198**, 108349 (2021).
- Zhu, C. et al. Silicon integrated microwave photonic beamformer. *arXiv: Optics*, (2020).
- Xie, Y. et al. Low-loss chip-scale programmable silicon photonic processor. *Opto-Electron. Adv.* **6**, 220030-220031-220030-220017 (2023).
- Testa, F., Pavesi, L. *Optical Switching in Next Generation Data Centers*. (Springer Publishing Company, Incorporated, 2017).
- Wetzstein, G. et al. Inference in artificial intelligence with deep optics and photonics. *Nature* **588**, 39–47 (2020).
- Li, N. et al. A Progress Review on Solid-State LiDAR and Nanophotonics-Based LiDAR Sensors. *Laser Photon. Rev.* **16**, 2100511 (2022).

16. Dupuis, N. & Lee, B. G. Impact of Topology on the Scalability of Mach-Zehnder-Based Multistage Silicon Photonic Switch Networks. *J. Lightwave Technol.* **36**, 763–772 (2018).
17. Cheng, Q. et al. Silicon Photonic Switch Topologies and Routing Strategies for Disaggregated Data Centers. *IEEE J. Sel. Top. Quantum Electron.* **26**, 1–10 (2020).
18. Zhao, W. et al. High-performance silicon polarization switch based on a Mach-Zehnder interferometer integrated with polarization-dependent mode converters. *Nanophotonics* **11**, 2293–2301 (2022).
19. Song, L. et al. Low-Loss Calibration-Free 2×2 Mach-Zehnder Switches With Varied-Width Multimode-Interference Couplers. *J. Lightwave Technol.* **40**, 5254–5259 (2022).
20. Kita, T. & Mendez-Astudillo, M. Ultrafast Silicon MZI Optical Switch With Periodic Electrodes and Integrated Heat Sink. *J. Lightwave Technol.* **39**, 5054–5060 (2021).
21. Chen, S., Shi, Y., He, S. & Dai, D. Low-loss and broadband 2×2 silicon thermo-optic Mach-Zehnder switch with bent directional couplers. *Opt. Lett.* **41**, 836–839 (2016).
22. Dong, P. et al. Submilliwatt, ultrafast and broadband electro-optic silicon switches. *Opt. Express* **18**, 25225–25231 (2010).
23. Zhang, C. et al. Wavelength-selective 2×2 optical switch based on a Ge₂Sb₂Te₅-assisted microring. *Photon Res* **8**, 1171–1176 (2020).
24. Huang, Y. et al. Multi-Stage 8×8 Silicon Photonic Switch Based on Dual-Microring Switching Elements. *J. Lightwave Technol.* **38**, 194–201 (2020).
25. Fegadolli, W. S. et al. Reconfigurable silicon thermo-optical ring resonator switch based on Vernier effect control. *Opt. Express* **20**, 14722–14733 (2012).
26. Qiao, L., Tang, W. & Chu, T. 32×32 silicon electro-optic switch with built-in monitors and balanced-status units. *Sci. Rep.* **7**, 42306 (2017).
27. Suzuki, K. et al. Low-Loss, Low-Crosstalk, and Large-Scale Optical Switch Based on Silicon Photonics. *J. Lightwave Technol.* **38**, 233–239 (2020).
28. Chu, T., Chen, N., Tang, W., Wu, Y. Large-Scale High-Speed Photonic Switches Fabricated on Silicon-Based Photonic Platforms. In: *Optical Fiber Communication Conference (OFC) 2023*. (Optica Publishing Group, 2023).
29. Xie, Y. et al. Thermally-Reconfigurable Silicon Photonic Devices and Circuits. *IEEE J. Sel. Top. Quantum Electron.* **26**, 1–20 (2020).
30. Soref, R. & Bennett, B. Electrooptical effects in silicon. *IEEE J. Quantum Electron.* **23**, 123–129 (1987).
31. Campenhout, J. V., Green, W. M. J. & Vlasov, Y. A. Design of a digital, ultra-broadband electro-optic switch for reconfigurable optical networks-on-chip. *Opt. Express* **17**, 23793–23808 (2009).
32. Selvaraja, S. K., Bogaerts, W., Dumon, P., Thourhout, D. V. & Baets, R. Subnanometer Linewidth Uniformity in Silicon Nanophotonic Waveguide Devices Using CMOS Fabrication Technology. *IEEE J. Sel. Top. Quantum Electron.* **16**, 316–324 (2010).
33. Dumais, P. et al. Silicon Photonic Switch Subsystem With 900 Monolithically Integrated Calibration Photodiodes and 64-Fiber Package. *J. Lightwave Technol.* **36**, 233–238 (2018).
34. Komma, J., Schwarz, C., Hofmann, G., Heinert, D. & Nawrodt, R. Thermo-optic coefficient of silicon at 1550 nm and cryogenic temperatures. *Appl. Phys. Lett.* **101**, 041905 (2012).
35. Quack, N. et al. Integrated silicon photonic MEMS. *Microsyst. Nanoengineering* **9**, 27 (2023).
36. Li, M., Tang, H. X. & Roukes, M. L. Ultra-sensitive NEMS-based cantilevers for sensing, scanned probe and very high-frequency applications. *Nat. Nanotechnol.* **2**, 114–120 (2007).
37. Li, M., Pernice, W. H. P. & Tang, H. X. Broadband all-photonic transduction of nanocantilevers. *Nat. Nanotechnol.* **4**, 377–382 (2009).
38. Han, S., Seok, T. J., Quack, N., Yoo, B.-W. & Wu, M. C. Large-scale silicon photonic switches with movable directional couplers. *Optica* **2**, 370–375 (2015).
39. Seok, T. J., Quack, N., Han, S., Muller, R. S. & Wu, M. C. Large-scale broadband digital silicon photonic switches with vertical adiabatic couplers. *Optica* **3**, 64–70 (2016).
40. Han, S. et al. Large-Scale Polarization-Insensitive Silicon Photonic MEMS Switches. *J. Lightwave Technol.* **36**, 1824–1830 (2018).
41. Han, S., Seok, T. J., Kim, C.-K., Muller, R. S. & Wu, M. C. Multicast silicon photonic MEMS switches with gap-adjustable directional couplers. *Opt. Express* **27**, 17561–17570 (2019).
42. Takabayashi, A. Y. et al. Broadband Compact Single-Pole Double-Throw Silicon Photonic MEMS Switch. *J. Microelectromechanical Syst.* **30**, 322–329 (2021).
43. Han, S. et al. 32×32 silicon photonic MEMS switch with gap-adjustable directional couplers fabricated in commercial CMOS foundry. *J. Opt. Microsyst.* **1**, 024003–024003 (2021).
44. Seok, T. J., Kwon, K., Henriksson, J., Luo, J. & Wu, M. C. Wafer-scale silicon photonic switches beyond die size limit. *Optica* **6**, 490 (2019).
45. Zhang, X., Kwon, K., Henriksson, J., Luo, J. & Wu, M. C. A large-scale microelectromechanical-systems-based silicon photonics LiDAR. *Nature* **603**, 253–258 (2022).
46. Quack, N., Seok, T. J., Han, S., Muller, R. S. & Wu, M. C. Scalable Row/Column Addressing of Silicon Photonic MEMS Switches. *IEEE Photonics Technol. Lett.* **28**, 561–564 (2016).
47. Nagai, T. & Hane, K. Silicon photonic microelectromechanical switch using lateral adiabatic waveguide couplers. *Opt. Express* **26**, 33906–33917 (2018).
48. Bulgan, E., Kanamori, Y. & Hane, K. Submicron silicon waveguide optical switch driven by microelectromechanical actuator. *Appl. Phys. Lett.* **92**, 101110 (2008).
49. Aharon, E. & Marom, D. M. Fast switching via frustrated total internal reflection in silicon photonics MEMS-actuated waveguides. In: *2019 International Conference on Optical MEMS and Nanophotonics (OMN)* (2019).
50. Jiang, X., Wu, H. & Dai, D. Low-loss and low-crosstalk multimode waveguide bend on silicon. *Opt. Express* **26**, 17680–17689 (2018).
51. Peng, Y., Li, H., Dai, D. Compact Silicon Photonic Waveguide Crossings with Sub-10-mdB Loss. In: *Asia Communications and Photonics Conference 2021* (eds Chang-Hasnain CWASWSPSYL-GEBERDD, Ma D). Optica Publishing Group (2021).
52. Aspelmeyer, M., Kippenberg, T. J. & Marquardt, F. Cavity optomechanics. *Rev. Mod. Phys.* **86**, 1391–1452 (2014).
53. Li, H., Chen, Y., Noh, J., Tadesse, S. & Li, M. Multichannel cavity optomechanics for all-optical amplification of radio frequency signals. *Nat. Commun.* **3**, 1091 (2012).
54. Li, H. & Li, M. Optomechanical photon shuttling between photonic cavities. *Nat. Nanotechnol.* **9**, 913–919 (2014).
55. Jo, G. et al. Wafer-level hermetically sealed silicon photonic MEMS. *Photon Res* **10**, A14–A21 (2022).
56. Tanizawa, K. et al. Ultra-compact 32×32 strictly-non-blocking Si-wire optical switch with fan-out LGA interposer. *Opt. Express* **23**, 17599–17606 (2015).

Acknowledgements

This work is funded by National Science Fund for Distinguished Young Scholars (61725503), National Natural Science Foundation of China (U23B2047, 6232116651, 92150302), Leading Innovative and Entrepreneur Team Introduction Program of Zhejiang (2021R01001), Zhejiang Provincial Major Research and Development Program (2021C01199), Natural Science Foundation of Zhejiang Province (LZ22F050006), Fundamental Research Funds for the Central Universities, and Startup Foundation for Hundred-Talent Program of Zhejiang University. The authors thank the ZJU Micro-Nano Fabrication Center and the Westlake Center for Micro/Nano Fabrication and Instrumentation for the facility support.

Author contributions

D.D. conceived the project. Y.H., Y.Sun, H.L., and D.D. designed the structures. Y.H. fabricated the devices. Y.H., and Y.L. characterized the devices. Y.H., H.L. and D.D. contributed to the data analyses. D.D., H.L., L.L., and Y.Shi managed the project. Y.H., H.L. and D.D. wrote the manuscript. All authors discussed the results and contributed to the manuscript.

Competing interests

D.D. and Y.Sun have a granted patent (grant number: CN110658584B/US11598921, PCT application number: PCT/CN2020/076340) on the silicon photonic MEMS switches based on split waveguide crossing presented in this paper. D.D., Y.Sun, and H.L. have a granted patent (grant number: CN112305676B) on the silicon photonic MEMS switches based on split waveguide crossing presented in this paper, which is also in progress of PCT patent application (application number: PCT/CN2021/078381). D.D., Y.H., and H.L. have filed a patent application (application number: CN116299874A) on the silicon photonic MEMS switches based on split waveguide crossing presented in this paper. The remaining authors declare no competing interests.

Additional information

Supplementary information The online version contains supplementary material available at <https://doi.org/10.1038/s41467-024-55528-9>.

Correspondence and requests for materials should be addressed to Huan Li or Daoxin Dai.

Peer review information *Nature Communications* thanks Keren Bergman and the other, anonymous, reviewer(s) for their contribution to the peer review of this work. A peer review file is available.

Reprints and permissions information is available at <http://www.nature.com/reprints>

Publisher's note Springer Nature remains neutral with regard to jurisdictional claims in published maps and institutional affiliations.

Open Access This article is licensed under a Creative Commons Attribution-NonCommercial-NoDerivatives 4.0 International License, which permits any non-commercial use, sharing, distribution and reproduction in any medium or format, as long as you give appropriate credit to the original author(s) and the source, provide a link to the Creative Commons licence, and indicate if you modified the licensed material. You do not have permission under this licence to share adapted material derived from this article or parts of it. The images or other third party material in this article are included in the article's Creative Commons licence, unless indicated otherwise in a credit line to the material. If material is not included in the article's Creative Commons licence and your intended use is not permitted by statutory regulation or exceeds the permitted use, you will need to obtain permission directly from the copyright holder. To view a copy of this licence, visit <http://creativecommons.org/licenses/by-nc-nd/4.0/>.

© The Author(s) 2024